Attitude Determination and Control System Design for a 6U CubeSat for Proximity Operations and Rendezvous

Francisco J. Franquiz [*], Peter Edwards [†] and Bogdan Udrea [‡]

Embry-Riddle Aeronautical University, Daytona Beach, FL, 32114, USA

Michael V. Nayak [§]

Red Sky Research, Albuquerque, New Mexico, 87108, USA

Thorsten Pueschl [¶]

dSPACE GmbH, Paderborn, 32102, Germany

The work presented in this paper focuses on the design of an attitude determination and control subsystem (ADCS) for a proximity operation and imaging satellite mission. The ARAPAIMA (Application for Resident Space Object Proximity Analysis and IMAging) mission is carried out by a 6U CubeSat class satellite equipped with a warm gas propulsion system. The propulsion system comprises a set of 16 reaction control system (RCS) thrusters, of 25 mN each, installed in pairs that generate torques about each of the satellite body axes and provide up to 100mN of thrust in two directions for orbital maneuvering. The thrust of the RCS thrusters can be modulated over the entire range in steps of 1% due to rapid solenoid valve actuation. The requirement of the control system is to provide pointing control accuracy of 1 arcmin at 3 σ in the desired imaging direction. The ADCS employs two control laws. One control law, for large angle maneuvers, implements eigenaxis maneuvering and the other, for accurate pointing, is implemented with PID controllers about each body axis.

Simulations performed for tracking the resident space object flying in a circular orbit of 500 km altitude from a relative orbit of 250 m are used to test the performance of the ADCS. A comparison between a "traditional" ADCS system with reaction wheels and RCS thrusters for their off-loading, and a system with only RCS thrusters has been performed. The accuracy of the pointing is comparable, the pointing performance as well as the propellant usage for both options are further discussed in the paper. The integration of both controllers within the ADCS and switching are also discussed.

Nomenclature

C_m	Moment coefficient
I_{sp}	Propellant specific impulse
J_p	Solar panel moment of inertia matrix
J_{rw}	Flywheel moment of inertia
K_m	Reaction wheel motor torque constant
Kn	Knudsen number
M_{sl}	Propellant slosh disturbance moment
N	Atomic nitrogen

---

[*]MS Candidate, Department of Aerospace Engineering, franquif@my.erau.edu
[†]MS Graduate, Department of Aerospace Engineering, edwardp1@my.erau.edu
[‡]Associate Professor, Department of Aerospace Engineering, udreab@erau.edu
[§]Principal Research Scientist, nayak@redskyresearch.org
[¶]Senior Application Engineer, tpueschl@dspace.de

American Institute of Aeronautics and Astronautics

O	Atomic oxygen
R_m	Reaction wheel motor resistance
S	Maximum projected satellite surface area
S_s	Sunlit surface area
T	RCS thrust
α	Angle of attack
β	Sideslip angle
$\boldsymbol{B_E}$	Earth's magnetic field vector at satellite location
$\boldsymbol{F_b}$	Force vector acting on the body-frame
$\boldsymbol{F_d}$	Disturbance force vector acting on the body-frame
$\boldsymbol{F_{cmd}}$	Controller Force Command
$\boldsymbol{H_{rw}}$	Reaction wheel angular momentum
$\boldsymbol{J_{rw}}$	Reaction wheel moment of inertia matrix
$\boldsymbol{J}$	Moment of inertia matrix
$\boldsymbol{M_b}$	Moment vector acting on the body-frame
$\boldsymbol{M_d}$	Disturbance moment vector acting on the body-frame
$\boldsymbol{M_{aero}}$	Aerodynamic disturbance moment
$\boldsymbol{M_{cmd}}$	Controller moment command
$\boldsymbol{M_{gg}}$	Gravity gradient disturbance moment
$\boldsymbol{M_p}$	Solar panel flexible mode disturbance moment
$\boldsymbol{M_{rmm}}$	Magnetic disturbance moment
$\boldsymbol{M_{srp}}$	Solar radiation pressure disturbance moment
$\boldsymbol{T_{cmd}}$	Controller thrust command at time
$\boldsymbol{V_\infty}$	Freestream velocity vector
$\boldsymbol{\Omega_{rw}}$	Reaction wheel angular velocity vector
$\boldsymbol{\Phi}$	Solar intensity vector
$\boldsymbol{\bar{\omega}}$	Angular velocity imaginary quaternion
$\boldsymbol{\bar{q}}$	Unit quaternion/Euler-Rodrigues parameters
$\boldsymbol{\dot{V}_b}$	Velocity vector of the body-frame
$\boldsymbol{\hat{e}}$	Euler-axis unit vector
$\boldsymbol{\hat{r}}$	Satellite position unit vector in the ECI frame
$\boldsymbol{\omega}$	Angular velocity vector of the body-frame
$\boldsymbol{\theta_p}$	Solar panel position vector
$\boldsymbol{m_{rmm}}$	Residual magnetic dipole or moment
$\boldsymbol{q_v}$	Vector quaternion component
$\boldsymbol{r}$	Satellite's position vector in the ECI frame
λ	Atmospheric particle mean free path
μ	Earth's gravitational parameter
ω_e	Earth's angular velocity vector
ω_{rw}	Reaction wheel angular speed
ϕ	Euler angle parameter
ρ	Mass density
θ_{sl}	Mechanical slosh model angular displacement
ξ	Reflectance value of the satellite
b	Solar panel joint damping coefficient
c	Speed of light in a vacuum
f_s	Average solar constant
f_{rcs}	RCS thruster operating frequency
g_e	Gravity at Earth's surface
h_{rw}	Reaction wheel nominal angular momentum
$h_{sl,n}$	Mechanical slosh model angular momentum
k	Solar panel joint spring constant
$k_{i,rw}$	Reaction wheel controller integral gain
$k_{p,rw}$	Reaction wheel controller proportional gain
l	Reference length (shortest satellite body dimension)

American Institute of Aeronautics and Astronautics

l_s	Solar radiation pressure moment arm
l_{rcs}	RCS thruster moment arm
m	Satellite rigid-body mass
$m_{b,rw}$	Propellant mass per reaction wheel off-load maneuvers
m_{prop}	Propellant mass
m_{sl}	Mechanical slosh model mass
n	Number density
q_0	Scalar quaternion component
s	Laplace transform complex parameter
$x_{sl,n}$	Mechanical slosh model linear displacement

I. Introduction

With the increasing interest in low budget space missions, academia has found a niche in the space industry. Going further than proposals and designs, many universities have flown satellites as parts of military and governmental initiatives across the world. A certain class of satellites, namely CubeSats (miniaturized satellites measured in 1 liter volume units or 1U), can be developed using commercial off-the-shelf (COTS) products which considerably lower the overall cost of missions. As the capabilities of CubeSat components continue to expand, mission designers take on tasks of increasing complexity.

A. Arapaima Mission Overview

By demonstrating robust, affordable, and responsive rendezvous and proximity operations of a nanosat with an uncooperative resident space object (RSO), the ARAPAIMA mission validates a range of technologies for space-based space situational awareness (SSA) and debris removal from Low Earth Orbit (LEO).[1] The ARAPAIMA mission proposes a reconnaissance approach to perform visible, infrared (IR), and 3D imaging of RSOs without a priori knowledge of their shape or attitude. This process follows a set of autonomous approach and close proximity maneuvers carried out with sufficient accuracy to allow rendezvous and docking maneuvers with the RSO.

The mission is carried out by a 12 kg 6U (36.6 x 23.9 x 27.97) cm CubeSat (with an imaging payload consisting of an IR camera, a miniature laser rangefinder, and a visible light monochrome camera arranged such that their respective imaging directions are parallel to each other as shown in Fig. 1.

To perform orbital approach maneuvers, the satellite is equipped with a difluoroethane warm gas propulsion system operated via rapid solenoid valve actuation and miniaturized 2D nozzle sets attached to the satellite body. The system comprises 16 RCS thrusters setup in pairs, each one capable of producing up to 25 mN of thrust. They are arranged such that, when operated in pairs, dual redundant torques can be exerted in both directions about each body-axis (Fig. 2). When operated in parallel, 4 nozzles allow for up to 100 mN of thrust in both direction of the x and z body-axes for orbital maneuvering.

The satellite's attitude determination and control system (ADCS) uses a combination of startracker (STR) and inertial measurement unit (IMU) to achieve a pointing control accuracy of 1 arcmin at 3σ in the desired direction of the imaging array (Fig. 1). The startracker has 6 arcsec accuracy about boresight and 40 arcsec off-boresight accuracy. The IMU includes angular rate gyro (150 °/s range) and accelerometer (± 2 g range) triads together with tri-axial magnetometer sensors (± 1.9 gauss). As a secondary attitude determination system, the satellite also carries photodiode sun sensors. The sun sensors are used during operational modes in which the startracker is unable to provide an attitude solution such as detumbling and sun acquisition maneuvers. An onboard GPS module is utilized to track the orbital position and velocity vectors of the satellite.

American Institute of Aeronautics and Astronautics

Legend:
B: Body-fixed frame
IRC: Infrared camera frame
L: Laser rangefinder frame
MC: Monochrome camera frame
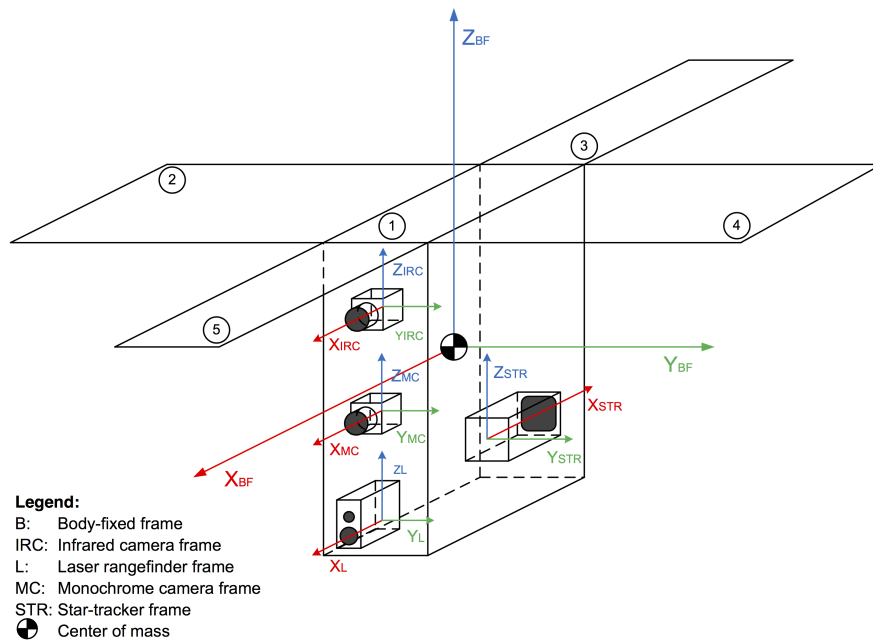STR: Star-tracker frame
⊕ Center of mass

Figure 1: Imaging array placement on the satellite body. The x-axis on the satellite body-fixed frame is defined as being parallel to the imaging direction.
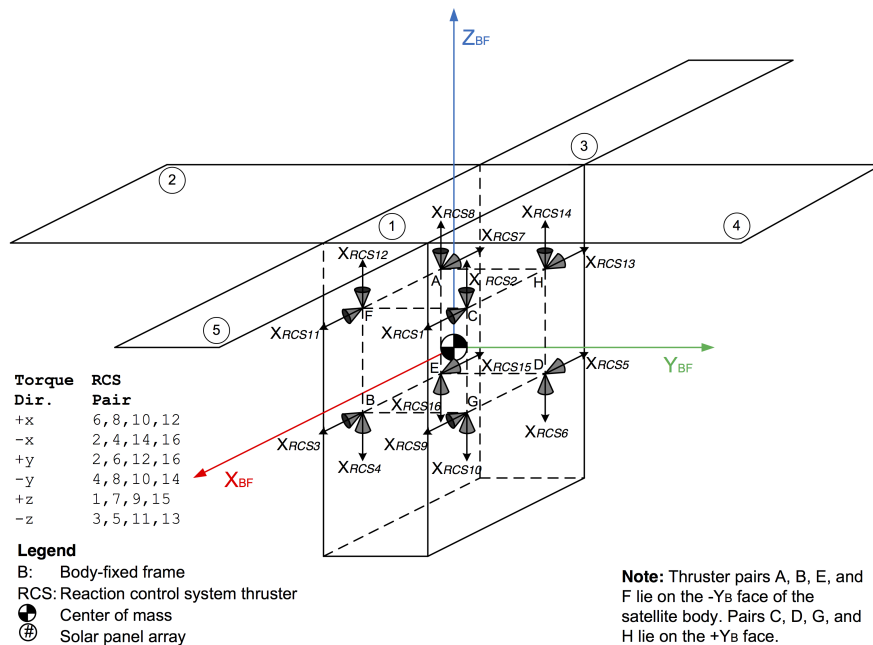

Torque Dir.	RCS Pair
+x	6,8,10,12
-x	2,4,14,16
+y	2,6,12,16
-y	4,8,10,14
+z	1,7,9,15
-z	3,5,11,13

Legend
B: Body-fixed frame
RCS: Reaction control system thruster
⊕ Center of mass
⊕ Solar panel array

Note: Thruster pairs A, B, E, and F lie on the $-Y_B$ face of the satellite body. Pairs C, D, G, and H lie on the $+Y_B$ face.

Figure 2: RCS thruster nozzle placement placement on satellite body-frame for a miniaturized propulsion system with dual redundancy. The nozzles are installed in pairs to opposing faces of the satellite bus.

American Institute of Aeronautics and Astronautics

II.   Dynamic Modeling

The dynamics of the satellite are modeled as those for a rigid body with 6 degrees-of- freedom (DOF) subjected to external (environmental) and internal disturbance torques and forces. The effect of the disturbances on the body are reflected as changes in the attitude of the body.

A.   Rigid-Body Dynamics

The satellite body is treated as a rigid body with constant mass and moment of inertia. The forces and moments acting on the satellite's body fixed frame are given by Eqs. (1) and (2) with the body-fixed frame defined with respect to the as shown in Fig. 2.

$$\boldsymbol{F_b} = m(\dot{\boldsymbol{V_b}} + \boldsymbol{\omega} \times \boldsymbol{V_b}) + \boldsymbol{F_d} + \boldsymbol{F_{cmd}}, \tag{1}$$

$$\boldsymbol{M_b} = \boldsymbol{J}\dot{\boldsymbol{\omega}} + \boldsymbol{\omega} \times (\boldsymbol{J}\boldsymbol{\omega}) + \boldsymbol{M_d} + \boldsymbol{M_{cmd}}. \tag{2}$$

All perturbations and inputs to the system are included directly into Eqs. (1) and (2) through the $\boldsymbol{F_d}$ and $\boldsymbol{M_d}$ terms respectively and are propagated through the integration of $\boldsymbol{\omega}$.

Changes throughout the mission to the satellite's configuration such as when appendages (solar panels, antennas, etc.) are deployed are modeled as impulsive changes in its moment of inertia by corresponding moment disturbances. Additionally, for the purpose of attitude control simulations the mass flow rate of the propellant is assumed to be sufficiently small for the mass to be considered constant throughout imaging maneuvers.

The attitude kinematics are described in terms of rotation quaternions. All quaternions referenced henceforth are considered to be normalized unit-quaternions and are defined as

$$\bar{q} = \begin{bmatrix} q_0 \\ q_1 \\ q_2 \\ q_3 \end{bmatrix} = \begin{bmatrix} \cos(\phi/2) \\ \sin(\phi/2)\hat{e}_x \\ \sin(\phi/2)\hat{e}_y \\ \sin(\phi/2)\hat{e}_z \end{bmatrix} = \begin{bmatrix} \cos(\phi/2) \\ \sin(\phi/2)\hat{e} \end{bmatrix} = \begin{bmatrix} q_0 \\ \boldsymbol{q_v} \end{bmatrix}, \tag{3}$$

where $\hat{e}$ is an arbitrary unit column vector and ϕ is an arbitrary angle through which a 3-dimensional frame is rotated about $\hat{e}$.

The quaternion kinematic equation in terms of the inertial-referenced body angular velocity is given by[2, 3]

$$\dot{\bar{q}} = \frac{1}{2}\bar{q} \otimes \bar{\boldsymbol{\omega}}, \tag{4}$$

where $\otimes$ indicates quaternion multiplication. In matrix notation

$$\dot{\bar{q}} = \frac{1}{2}\boldsymbol{\Omega}(\boldsymbol{\omega})\bar{q}, \tag{5}$$

where

$$\boldsymbol{\Omega}(\boldsymbol{\omega}) = \begin{bmatrix} 0 & -\omega_x & -\omega_y & -\omega_z \\ \omega_x & 0 & \omega_z & -\omega_y \\ \omega_y & -\omega_z & 0 & \omega_x \\ \omega_z & \omega_y & -\omega_x & 0 \end{bmatrix}. \tag{6}$$

Equations (1) and (2) along with Eq. (4) make up the full dynamics of the model and allow the satellite's state to be determined at any time t based on known initial conditions.

The error quaternion of the satellite is defined as the quaternion which describes the rotation from the current quaternion state to the commanded quaternion and is defined as

$$\bar{q}_e = \begin{pmatrix} q_{0,e} \\ \boldsymbol{q_{v,e}} \end{pmatrix} = \bar{q}_{cmd}^{-1} \otimes \bar{q}. \tag{7}$$

American Institute of Aeronautics and Astronautics

The pointing angle error is defined as the angle from the body x-axis (imaging direction) to the desired x-axis as given by the error quaternion. It can be easily calculated as

$$\psi_e = (q_{0,e}^2 + q_{1,e}^2 - q_{2,e}^2 - q_{3,e}^2). \tag{8}$$

B.   External Disturbance Models

To account for environmental conditions set of models are set parallel with the dynamic equations discussed above. These shape the moments and forces acting on the system to mirror the scenario of a detumbled satellite in a 28.5° inclination LEO at approximately 500 km from the Earth's surface. At this altitude, the effects of Earth's gravitational and magnetic field as well as its atmosphere are non-negligible.[4] As such, they form the majority of the plant or process under consideration.

At this point in time it would also be useful to specify the reference frames utilized throughout the different models. The body frame has already been defined as seen in Figs. 1 and 2. The inertial frame is defined as the ECI (Earth-Centered Inertial) as described by the J2000 system.[5] This frame is used for all internal calculations throughout the models and it serves as a reference point for transformations between different frames. Another useful frame is the ECEF (Earth-Centered Earth-Fixed) which rotates with the Earth.

Finally, some environmental models provide information on the North-East-Down (NED) frame, a type of noninertial, flat Earth (local tangent plane, LTP) reference system usually used for aircraft navigation.[6] In this system the x-axis points to the polar North (parallel to the LTP) while the z-axis points downward (nadir), towards the Earth's surface. The y-axis completes the right-handed frame and points East on the LTP (Fig. 3). Note that while the center of the NED frame is dependent on the body's location (relative to ECEF) the frame is not a body-fixed frame. All results in this section are shown in the satellite body-fixed frame relative to the ECI frame at January 1st, 2015.
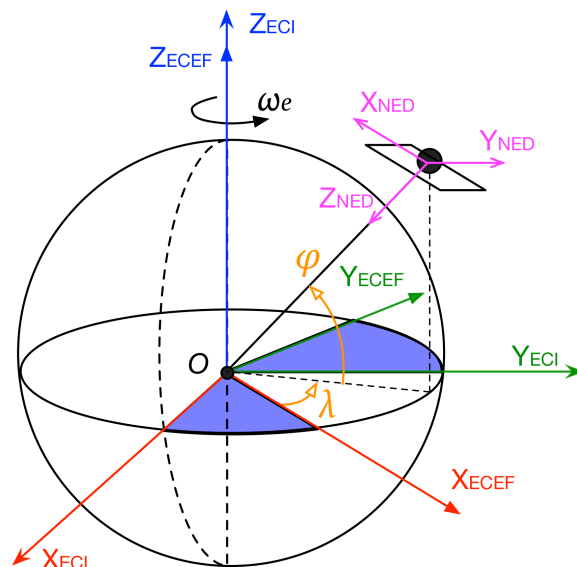

Figure 3:   ECI, ECEF, and NED reference frames. The latitude (λ) and longitude (ϕ) convention for an arbitrary point over the Earth's surface with respect to the ECEF frame is shown.

1.   Aerodynamic Drag

At LEO, the atmospheric density and composition have a direct impact on the satellite's attitude especially when one considers its low mass and the size of the solar panels relative to the body. Using the MSISE90 atmospheric model it is possible to estimate the density, temperature, and composition of the atmosphere as well as the number densities of its components at a specified altitude on the ECEF.[7] Data from the NRLMSIS-00 (an updated version of MSISE90) is also used since it contains additional data on Oxygen particles at altitudes above 500 km.[8]

Aerodynamic torques are produced by the atmospheric particles colliding with the satellite surface. Collisions occur at a higher frequency during maximum solar activity resulting in larger disturbances. This worst case scenario has been assumed for all aerodynamic calculations. The aerodynamic torques acting on the satellite are estimated by Eq. (9)

$$\boldsymbol{T_{aero}} = \frac{1}{2}\rho\boldsymbol{V}_\infty^2 C_m Sl. \tag{9}$$

American Institute of Aeronautics and Astronautics

At a nominal altitude of 500 km the NRLMSISE00 model gives an atmospheric composition of 94% O and 6% N. The number and mass densities are $n = 3.769 \times 10^{14}$ kg\m^{-3} and $\rho = 1.02 \times 10^{11}$ kg\m^{-3} respectively and the temperature is 1491 K. The mean free path between particles $\lambda = 27.33$ km which compared with a reference length l of 0.1 m results in a Knudsen number, $Kn = \lambda/l = 273,300$, indicating that the satellite operates in the free molecular flow regime.

Given the previous statement, the moment coefficients of the satellite were calculated using the direct solution Monte Carlo (DSMC) program DAC97, which employs algorithms based on the methods described by G.Bird.[9] A variable hard sphere model (VHS) has been assumed for the collisions between the particles (O and N) and the satellite. V_∞ has been assumed to be 7.612 km\s, which is equivalent to the mean orbital speed at a 500 km circular orbit.
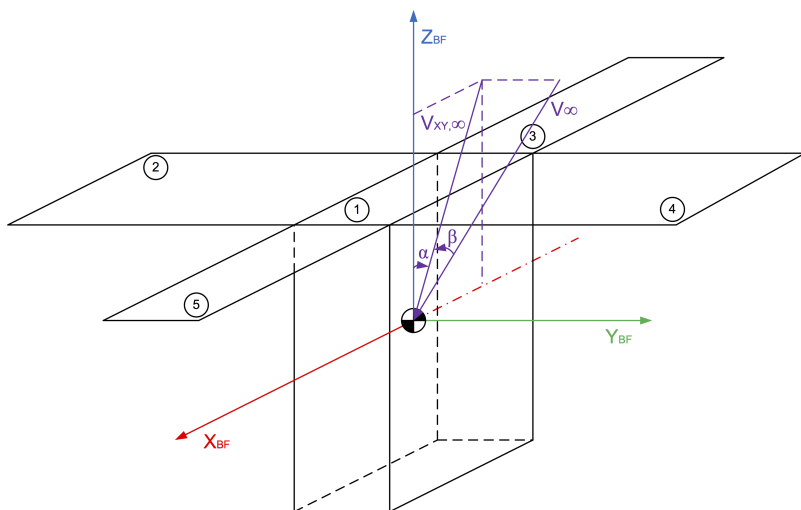
Figure 4: Angle of attack (α) and angle of slip (β) definitions for the aerodynamic drag on the satellite body-frame. These provide the orientation for the flow direction in the DSMC iteration results.
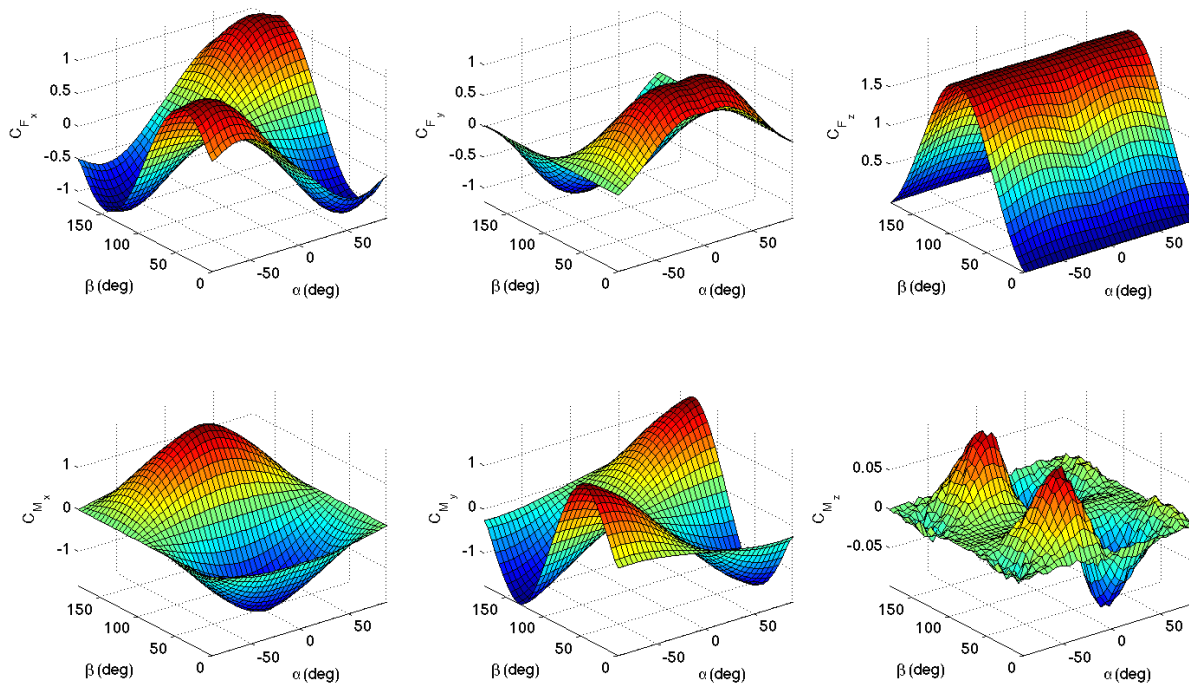
Figure 5: Force and moment coefficients of the ARAPAIMA satellite as functions of its orientation in terms of α and β. The first three plots describe the change of the force coefficient in the x, y, and z body-axes respectively. The following three plots do the same for the moment coefficients.

American Institute of Aeronautics and Astronautics

A total of 1369 runs of the DAC97 code have been performed on the ARAPAIMA body geometry for 37 different α and β values. The angle of attack was varied between -90° and 90° in steps of 5°; the sideslip angle was similarly varied between 0° and 180° (the angle of attack and the sideslip angle are defined as seen in Fig. 4). The DSMC results are used to form 2D look-up tables which map the drag and moment coefficients as functions of α and β as shown in Fig. 5. Together with the total mass density obtained from the MSISE90 model Eq. (9) is used to calculate the aerodynamic disturbance torques at any orientation (Fig. 6(a)). The maximum force coefficient corresponding to the drag coefficient in general aerodynamic terms is approximately 2.0 which is within the expected range (2.0-2.2) for small satellites in LEO.[4]

2. Magnetic Residual Moment

The magnetic disturbance torque has two major sources: the force produced on a point charge by the magnetic component of the Lorentz force, and the torque experienced by an aspheric paramagnetic body which, in the absence of other torques, aligns its long axis with the local magnetic field. This means that all electrically conducting parts of the satellite contribute charges and produce time varying magnetic fields. Due to the complex nature of evaluating these disturbance torques, empirical data is used to estimate their effect.

The Earth's magnetic field is predicted using the 2010-2015 World Magnetic Model (WMM), which provides magnetic intensity, inclination, declination, and a complete geometry of the field at any point in a -1 km to 850 km range (z-direction)in the NED frame.[10] An estimate of the maximum magnetic torque can then be obtained by combining all contributing magnetic effects into a residual dipole moment specific to the satellite body and exposing it to the environmental magnetic field[4,11]

$$T_{rmm} = m_{rmm} \times B_E. \tag{10}$$

For the ARAPAIMA satellite, m_{rmm} was approximated to be 0.1 A m^2 aligned with the body y-axis thus $m_{rmm} = [0, 0.1, 0]$ A m^2. The resulting M_{rmm} can be calculated as shown in Fig. 6(b).

3. Gravity Gradient Torque

In order to have the body follow an orbital trajectory, a gravitational model of Earth is used to determine the force acting on the satellite at any point in time. The model implements the mathematical representation of the geocentric equipotential ellipsoid described by the 1984 World Geodetic System (WGS84).[3]

When the center of mass of a satellite does not coincide with its center of gravity, the variation of the Earth's gravitational field over the volume of the spacecraft produces torques which in the absence of other disturbances will try to align one of the body's principal axes with the local gravity field vector.[12] This disturbance is given by

$$M_{gg} = \frac{3\mu}{|r|^3}(\hat{r}) \times J\hat{r}. \tag{11}$$

The gravity gradient disturbance contribution to the attitude dynamics can be calculated by evaluating Eq. (11) along the satellite's trajectory. The resulting moments are shown in Fig. 6(c).

4. Solar Radiation Pressure

When solar photons collide with a satellite, the momentum exchange between sunlight and the body surface results in a net pressure force called solar radiation pressure. This pressure is a complex function of the shape and optical properties of the satellite as well as the shading and solar intensity Φ. The worst case scenario is given by Eq. (12) where Φ is taken from an STK simulation for the day of January 1st, 2015

$$M_{srp} = \frac{\Phi f_s S_s (1 + \xi) l_s}{c}. \tag{12}$$
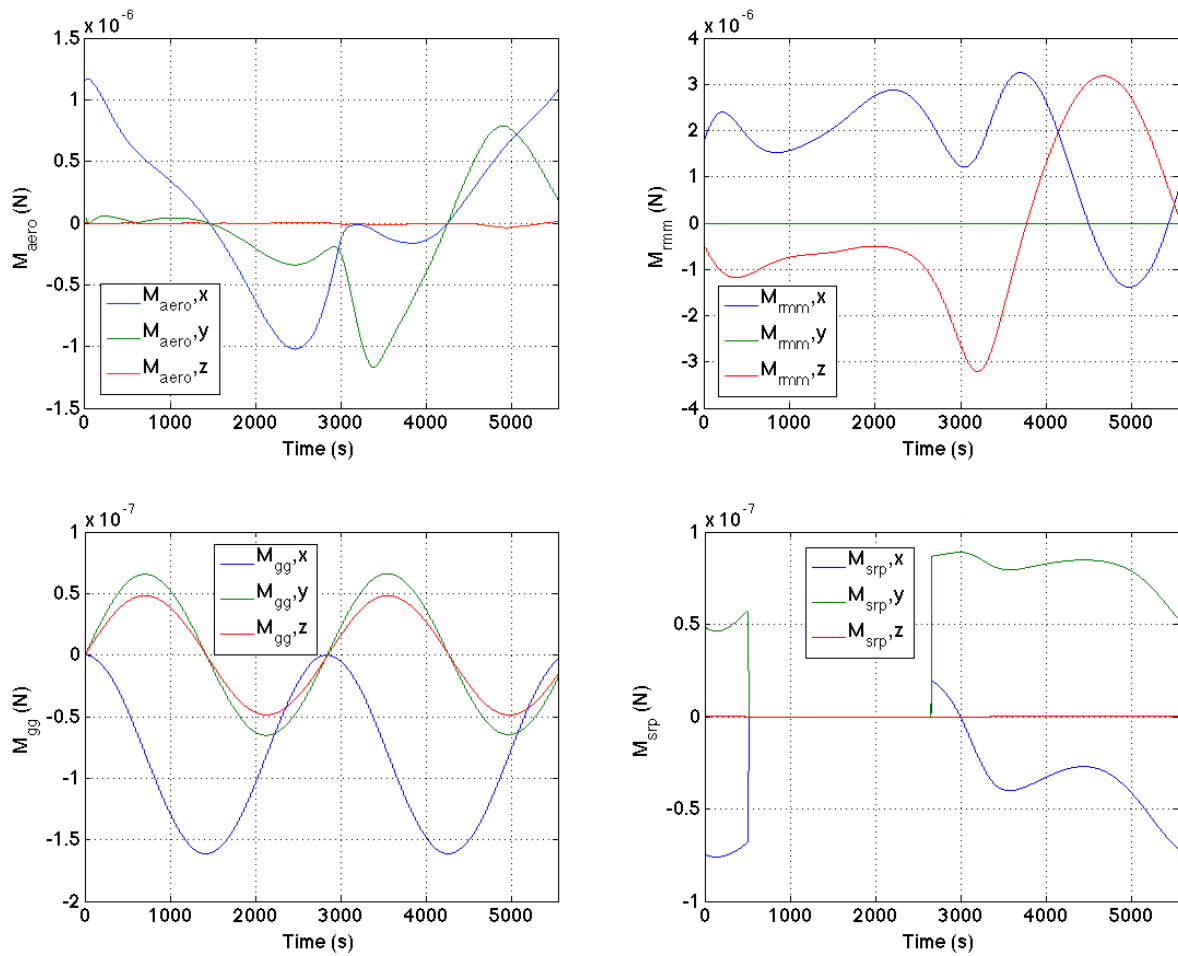
The resulting moment is shown in Fig. 6(d).

Figure 6: Aerodynamic (top-left), magnetic residual (top-right), gravity gradient (bottom-left), and solar radiation pressure (bottom-right), external disturbance torques acting on satellite body for a 1 orbit period. Note: The solar radiation pressure is zero for the portion of the orbit spent in eclipse.

C. Internal Disturbance Models

External factors are not the only sources of disturbances for a satellite; moving parts and other mechanical interfaces also produce undesirable torques. Many of these internal disturbances are also produced or exacerbated as a result of active control. Because there is no ideal way to mitigate them, the controller must be able must be able to minimize both external and internal torques.

1. Solar Panel Flexible Modes

In order to deploy properly, the solar panel hinges are loaded with springs which rotate upon release. In order for the rigid body dynamics outlined in section A to be valid the flexible joints must be modeled such that any moment or force resulting from their movement can be folded into the pre-existing dynamic equations. Given the solar panels are rigid bodies, the joints can be modeled as torsion springs by

$$\boldsymbol{M_p} = \boldsymbol{J_p}\ddot{\boldsymbol{\theta}}_{\boldsymbol{p}} + b\dot{\boldsymbol{\theta}}_{\boldsymbol{p}} + k\boldsymbol{\theta_p}. \tag{13}$$

The resulting moment $\boldsymbol{M_p}$ can now simply be added to Eq. (2) as a disturbance. Although small in comparison to the external disturbances (Fig. 7), modeling this reaction is important in order to monitor and avoid exciting structural modes through control actuation.

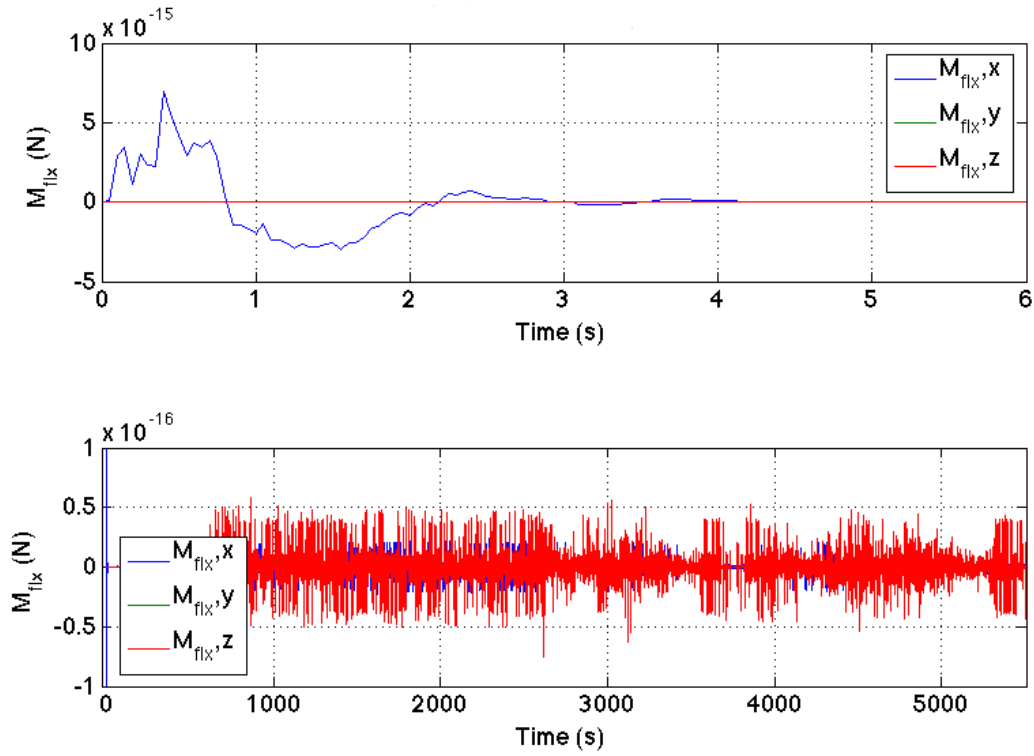American Institute of Aeronautics and Astronautics

Figure 7: Flexible solar panel disturbance moment. The top plot shows the initial jump at the time of deployment, the bottom shows flex disturbance for the duration of an orbit.

2. Propellant Slosh

Even in microgravity, liquid propellant slosh contributes directly to attitude destabilization. In the case of the ARAPAIMA mission, slosh can hinder mission completion by introducing unwanted angular momentum which could result in a deviation from trajectory during orbital maneuvers or in oscillations of the pointing axis which prevent sufficiently stable imaging. For this reason, a simple yet fairly accurate spring-mass-damper equivalent mechanical model was incorporated in the simulation. This model takes into account the propellant's behavior through the Weber, Froude and Bond numbers and results in the following moment equation proposed by Dodge[13] in terms of angular (θ_{sl}) and linear (x_{sl}) displacements

$$M_{sl} = -(J_{x,0} + m_{sl,0}h_0^2)\theta_{sl} - \sum^{n} m_{sl,n}h_{sl,n}(\ddot{x}_{sl,n} + H_{sl,n}\theta_{sl,0}) + g\sum^{n} m_{sl,n}x_{sl,n}. \tag{14}$$

Where the summations correspond to the combined effect of the different slosh modes in the mechanical model. Note that, due to the nature of the mass-spring-damper representation Eq. (14), needs to be modified according to the expected motion along each axis (especially depending on the alignment of the thrusters). The x-axis implementation is given above. The output on all three axes for one orbit can be seen in Fig. 8.

D.   Actuator Model

Originally the ARAPAIMA mission relied on reaction wheels to perform attitude control, however, these were still dependent on the RCS thrusters in order to periodically despin the flywheels. This dependency coupled with volume, mass, and power constraints led to the decision of eliminating the reaction wheels in favor of an RCS thruster actuated control system. A trade study focusing on propellant consumption and attitude performance was made to ensure the change would not affect the satellite's ability to complete the mission.
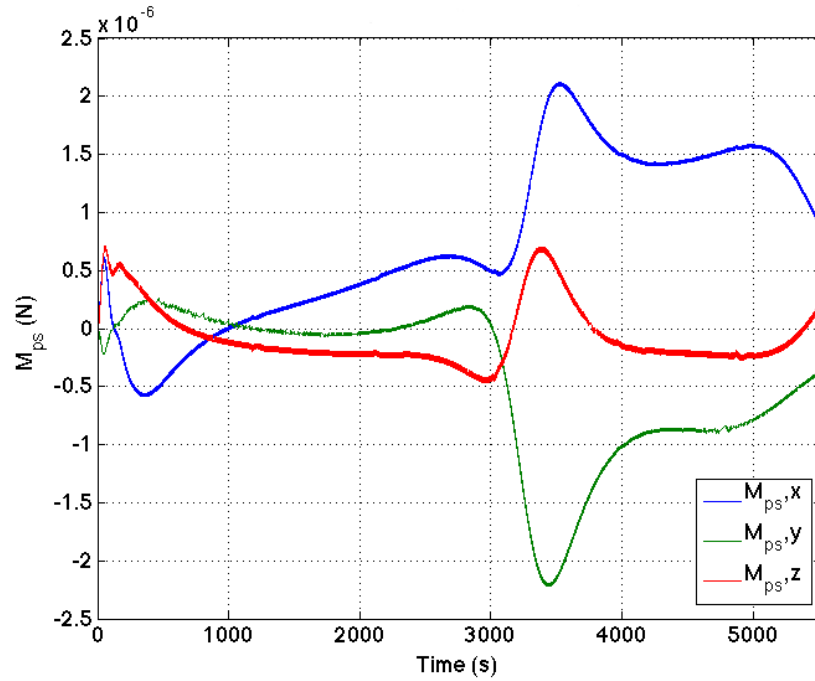
American Institute of Aeronautics and Astronautics

Figure 8: Propellant slosh disturbance moment.

1. Reaction Wheels

The reaction wheels (RWs) were modeled as brushed DC motors with an open-loop transfer function given by

$$\frac{\omega_{rw}}{V} = \frac{K_m}{(R_m J_{rw})s + K_m^2} = \frac{K}{\tau s + 1}. \tag{15}$$

Where the mechanical parameters are as follows: motor torque constant $(K_m) = 7.12 \times 10^{-3}\,\mathrm{N\,m/A}$, armature resistance $(R_m) = 7.12\,\Omega$, and the total RW moment of inertia $(J_{rm}) = 5.11 \times 10^{-5}\,\mathrm{kg\,m^2}$. Adding a simple PI controller yields the following closed loop transfer function

$$\frac{\Omega_{rw}}{V} = \frac{K k_{i,rw}}{\tau s + (K k_{p,rw} + 1)s + K k_{i,rw}}. \tag{16}$$

Where the tuning parameters are set as $k_p = 1.66$ and $k_i = 54.76$. The reaction wheel angular momentum can be calculated as

$$\boldsymbol{H_{rw}} = \boldsymbol{J_{rw}} \boldsymbol{\omega_{rw}},$$

then the torque applied to the satellite is given as a function of its angular velocity

$$\boldsymbol{M_{rw}} = \boldsymbol{\Omega} \times \boldsymbol{H_{rw}}. \tag{17}$$

The propellant usage needed to offload the reaction wheels is determined by calculating the required thruster burn time and the saturation time of each reaction wheel. The burn time is dependent on the mass flow rate $\dot{m_{prop}}$ and specific impulse I_{sp} of the propellant. The saturation time is dependent on the reaction wheel nominal angular momentum and the root square sum of the disturbance torques acting on the satellite body

$$t_{burn} = \frac{h}{2Tl_{rcs}}, \tag{18}$$

$$\dot{m}_{prop} = \frac{T}{I_{sp} g_e}. \tag{19}$$

American Institute of Aeronautics and Astronautics

Thus the amount of propellant used per offload maneuver is calculated by

$$m_{b,rw} = \dot{m}_{prop}t_{burn}. \tag{20}$$

For a disturbance scenario corresponding to that shown in Fig. 6, evaluating Eq. (20) over time estimates a total of 0.945 g of propellant per orbit needed to offload the reaction wheels. Note that this is a worse case scenario which assumes constant imaging mode pointing requirements (1 arcmin).

2. RCS Thrusters

Using pulse width modulation techniques the thrusters can be "throttled" at 1% increments of the maximum thrust value over a linear region made possible by rapid solenoid valve actuation. When operated within a range of 0-60 Hz, the mass flow rate remains linear through the entire duty interval (Fig. 9). When operated at higher frequencies the linear region begins to deteriorate; the current model assumes a $f_{rcs} = 10$ Hz operating frequency.

Building on these properties the RCS thruster model assumes a quantized linear relationship between the commanded and produced thrust where each step size corresponds to a 1% of the maximum thrust value. A graphical representation of this assumption is shown in Fig. 10.

This quantized model also introduces a delay which corresponds to the difference in sampling time of the controller, valves, and onboard computer. Because the current simulation assumes the valves operate at a slower frequency than the controller, this delay is currently equivalent to $\frac{1}{f_{rcs}}$. Equation (21) describes the relationship between the commanded and delayed actuated moment
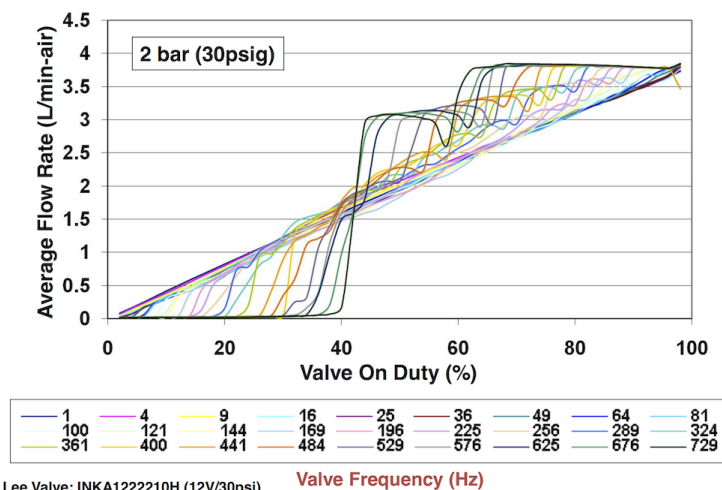

Figure 9: RCS valve performance in terms of the mass flow rate relation to duty cycle at different operation frequencies. This relation remains linear on a range of 0-60 Hz.[14]
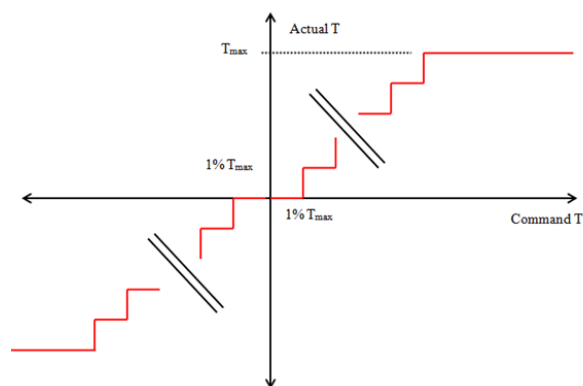
$$\begin{aligned} \boldsymbol{M_{cmd,(t)}} &= 2l_{rcs}\boldsymbol{T_{cmd,(t)}} \\ \boldsymbol{M_{act,(t+1)}} &= 2l_{rcs}\boldsymbol{T_{act,(t+1)}} &= 2l_{rcs}\boldsymbol{T_{cmd,(t)}} \end{aligned}. \tag{21}$$

As a means of direct performance comparison with the reaction wheel actuated control, the same disturbance scenario was presented to the thruster actuated system. The total propellant per orbit needed to reject all exterior disturbances was approximately 1 g as shown in Fig. 11. Figure 12 compares the pointing performance of both actuators. Given that the pointing performance of both actuators is comparable and the propellant usage is the same for this combination of thrust and propellant specifications, the RWs were removed from the design in order to save mass and volume needed for other components.

American Institute of Aeronautics and Astronautics

Figure 10: 1% of maximum thrust quantization and saturation of thrust command values fpr the RCS thruster valves.
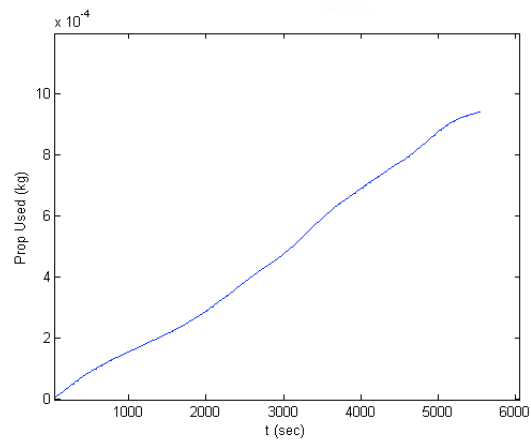

Figure 11: Propellant usage for disturbance rejection using the RCS thrusters alone for a 1 orbit period.
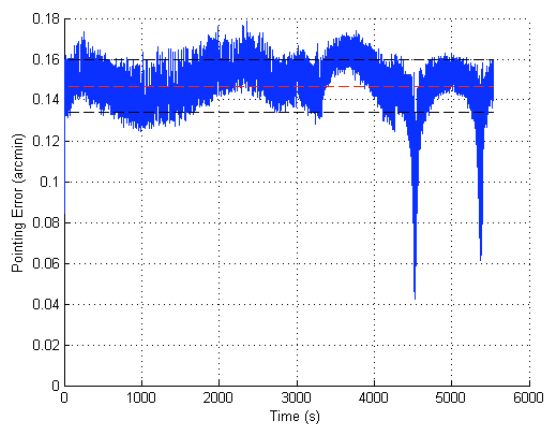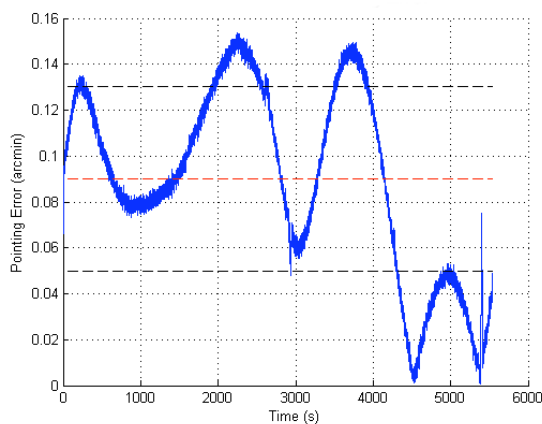

Figure 12: RW (left) and RCS thruster (right) pointing performance when subjected to the disturbances shown in Fig. 6.

American Institute of Aeronautics and Astronautics

III. Controller Design

The ARAPAIMA mission requires that its ADCS be able to handle long angle transition maneuvers as well as precise attitude tracking imaging maneuvers. Figure 13 illustrates how the satellite must maneuver towards, then acquire and maintain a circular orbit (250 m) relative to the RSO while keeping the payload pointed at the RSO for imaging. The control approach presented here uses a combination of nonlinear eigenaxis control and PID controllers about each axis. For the moment, a periodic switching scheme is presented together with a bump conditioning algorithm with scheduled gains which attempts to smooth the transition between controllers.

A. Eigenaxis Control

The large angle maneuver control law is based on the quaternion feedback regulator proposed by Wie[15] and applied by Pong[16] to CubeSat missions. The controller consists of a linear error quaternion feedback and both linear and nonlinear angular rate feedback which counteract gyroscopic coupling torques.[15] This approach is based on eigenaxis rotations and is analogous to the well known PD controller. It was designed for large angle maneuvers and its global stability as well as its robustness to
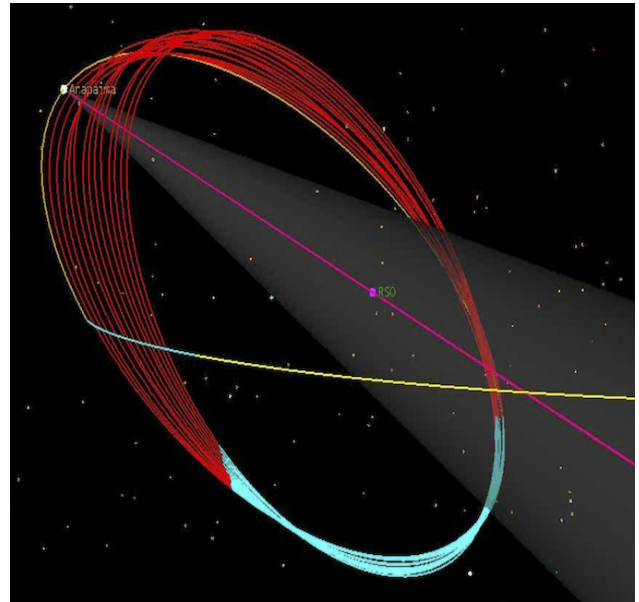

Figure 13: STK illustration of a circular relative orbit acquisition. The approach path is shown in yellow and the acquisition and maintenance maneuvers are shown in light blue. The red line shows the path for a 250 m circular orbit around the RSO for approximately 1 day.

inertia matrix uncertainty has been proven in relation to various spacecraft applications.[15,17,18] The torque command given by the control law is expressed as

$$M_{cmd} = -\omega \times J\omega - K_d\omega - K_p\bar{q}_e, \tag{22}$$

where the proportional and derivative gain matrices are given by $K_p = pJ$ and $K_d = dJ$ respectively; p and d are scalar tuning parameters.

B. PID Control

As with all PD controllers, the lack of an integral term introduces non-zero steady state errors. In order to achieve the high accuracy needed for imaging modes, a simple PID controller is applied about each axis. Taking the vector part of the error quaternion

$$M_{cmd} = -[K_p + \frac{K_i}{s} + K_d s]q_{e_v}, \tag{23}$$

where the gains again are the product of the body moment of inertia matrix and scalar tuning parameters.

However, integral controllers are ill suited for large angle maneuvers and are heavily dependent on the magnitude of the error or initial conditions to ensure stability. Therefore, the PID control law is implemented as an extension of the eigenaxis controller which comes into effect once a certain set of circumstances are met. These circumstances are a weighed combination of the current attitude error, its behavior over time, and the current mission operational mode. This way, the eigenaxis controller operates throughout the majority of the maneuvers and ensures the appropriate conditions are met for the PID controller to take over.

American Institute of Aeronautics and Astronautics

1. Bump Conditioning

The smoothness with which the switch or transfer between controllers occurs is addressed by considering bump conditioning techniques as presented by Peng.[19] Although complex system dynamics prevent completely bumpless transitions, some improvement is achieved by altering Eq. (23) to the following form:

$$M_{cmd,t2} = -K_p q_{e_v,t1} - \frac{K_i}{s}[K_t(M'_{cmd,t1} + M_{cmd,t1}) + q_{e_v,t1}] - K_d s q_{e_v,t1}. \tag{24}$$

Note that the difference between Eq. (23) and Eq. (24) lies on how the integral action is addressed. Because the eigenaxis controller lacks integral terms, this kind of conditioning in only useful when switching to PID control; similar corrections are unnecessary when operation switches back to eigenaxis control.

The effectiveness of Eq. (24) can be augmented by the use of scheduled gains. Building on the notion that integral controllers are sensitive to abrupt changes, linear transitions can be scheduled such that the gain values are identical to those of the eigenaxis controller at the instant when the switch to PID occurs. This further smooths the introduction of integral action into the system since K_i would start at zero and then increase according to some continuous linear function of time $f(t)$ as:

$$\begin{aligned} p_2 &= p_1 + f(t)(p_2 - p_1) \\ i_2 &= i_1 + f(t)(i_2 - i_1) \\ d_2 &= d_1 + f(t)(d_2 - d_1) \end{aligned} \tag{25}$$

where $f(t)$ ranges from 0 to 1. The slope of $f(t)$ then controls the abruptness of the transition.

IV.   Numerical Simulation and Results

A numerical simulation model has been prepared in a combined MATLAB and Simulink environment. This setup has the advantage of including many blocksets and functions which simplify the calculations needed, particularly the built-in interface for the environmental models mentioned in section B. The model runtime was set to simulate a single 92 min orbit in close proximity (250 m) to the RSO using a 4th order fixed-step extrapolation integrator (ode14x) with a step size of 0.05 s. The integrator, based on a linearly implicit Euler method, was chosen for its robustness in solving stiff differential-algebraic problems. The RSO and satellite orbits were determined from STK simulations used to design the ARAPAIMA mission trajectories. These provide the required ω_{cmd} and $\bar{q}_{cmd}$ commands needed to track the RSO (i.e. controller commands).
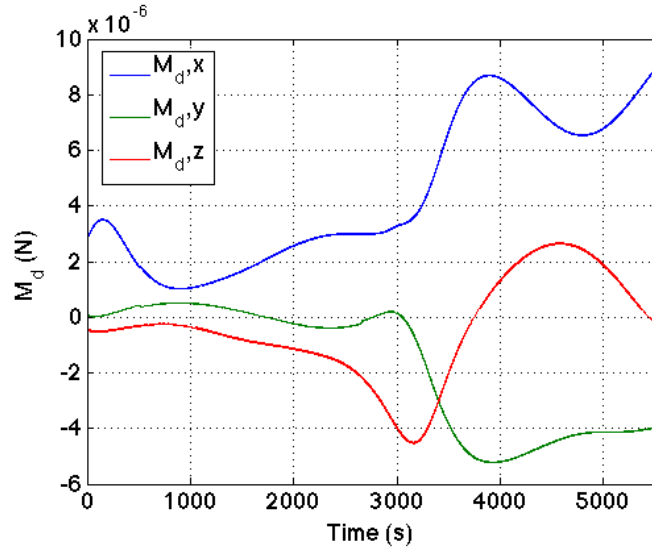

Figure 14: Total moment on the satellite body resulting from the combined effects of external and internal disturbance torques throughout 1 orbit.

American Institute of Aeronautics and Astronautics

The model takes into account all dynamics outlined in section II and applies both control laws discussed in section III. However, due to the short span of the simulation, the switching between controllers has been made periodic in order to show the characteristics of both control laws. Figure 14 shows the combined internal and external disturbance torques acting on the body throughout the simulation. For the purposes of initializing all environmental models, the date is assumed to be January 1st 2015. This date also corresponds to the date of the RSO orbit simulation.

The eigenaxis controller is tuned so that the scalar tuning parameters $p_1 = 8$, $d_1 = 0$, and $i_1 = 0$ whereas the PID controller was tuned so that $p_2 = 2$, $d_2 = 15$, and $i_2 = 0.1$. Figure 16 shows the overall pointing performance of the satellite for different control settings. In order to assess the advantages of switching while still quantifying the smoothness of the transition between controllers three different scenarios are examined. The first (Fig. 16, subfigure (a)) shows the pointing performance with no bump conditioning or gain scheduling. This gives a steady state error of 0.18 arcmin for the eigenaxis controller and 0.025 for the PID controller. However, the switch causes significant overshoot (1-7 arcmin). Note that the PID is sensitive to changes in angular acceleration whereas the eigenaxis controller remains at steady state except for short jumps where the accuracy improves.

The second scenario (subfigure (b)) shows the performance when the PID controller is as in Eq. (24). This offers noticeable improvement in the switch overshoot (0.65-3 arcmin) but because the K_t term remains non-zero after the transient period, it offers no improvement on the overall performance. This is fixed in the third scenario when gain scheduling is introduced. The scheduled gains assume a transient period of 200 s during which the $\boldsymbol{K_p}$, $\boldsymbol{K_i}$, $\boldsymbol{K_d}$ gains are changed according to Eq. (25) and are shown in Fig. 15. The bump conditioning gain does not behave this way, but instead is a fixed non-zero value during the transient period and is zero elsewhere. This approach further improves the overshoot (0.70-1.20 arcmin) and restores the improvement on pointing performance seen in the first scenario yet at the cost of longer transition periods. Subfigure (d) gives a side by side comparison of the bump conditioning given by each approach.
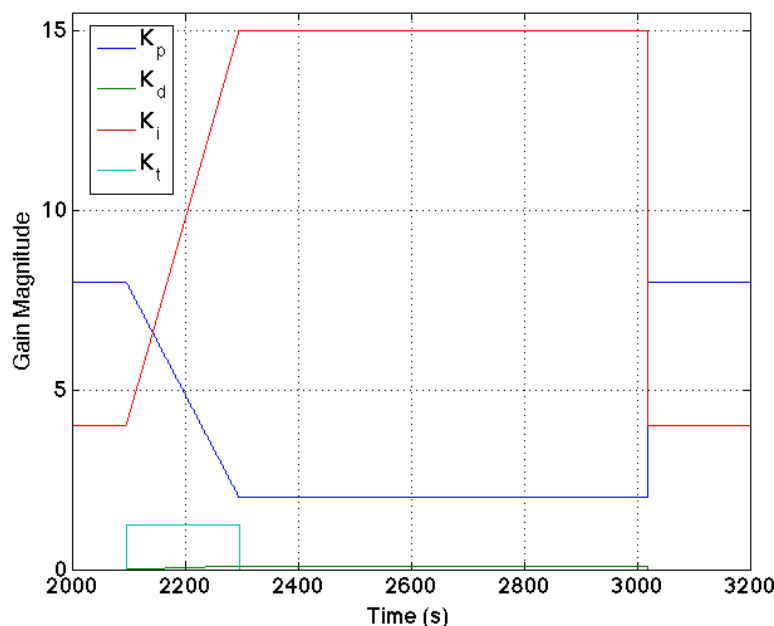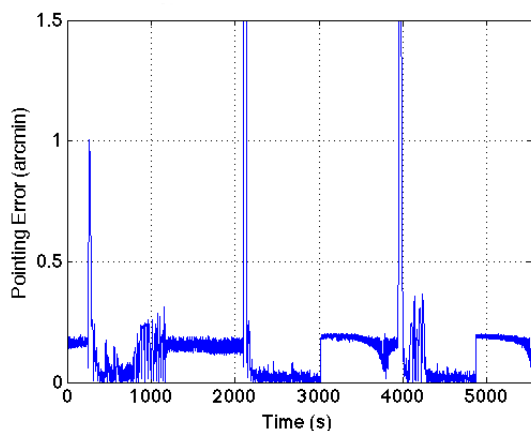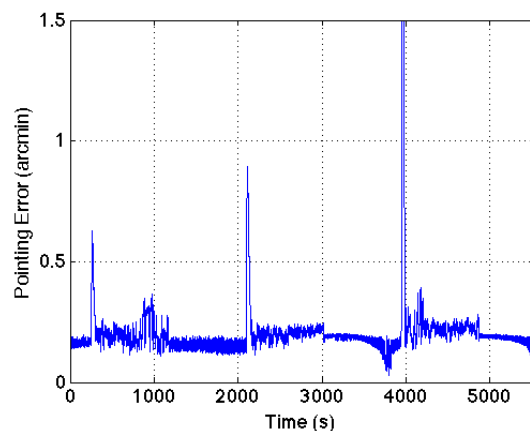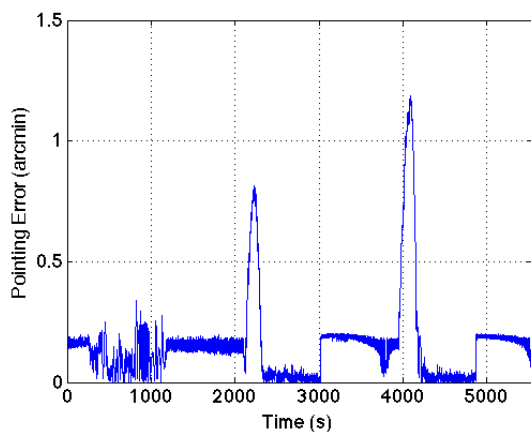

Figure 15: Gain scheduling transients corresponding to the switch shown in figure 16(d).

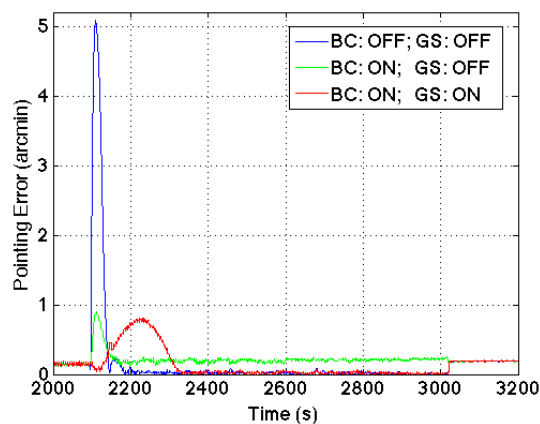American Institute of Aeronautics and Astronautics

(a) Pointing performance with no bump conditioning and no gain scheduling

(b) Pointing performance with bump conditioning but no gain scheduling

(c) Pointing performance with bump conditioning and gain scheduling.

(d) Bump conditioning performance comparison. BC and GS correspond to bump conditioning and gain scheduling respectively.

Figure 16: Switching controller performance.

A. Future Work

While current results are promising, there remain ways in which the fidelity of the model might be improved in order to further test and prove the stability of the ADCS. As the control laws must be implemented on the satellite's on-board computer, the entire model must be discretized and made to account for the different sampling rates and inherent delays of digital implementation. In direct relation is the matter of hardware noise and interference along with a corresponding filter design to compensate for the rate transition and inaccuracies of sensor readings. Figure 17 gives an example of controller performance with unfiltered sensor noise; the noise levels are based on the real mission hardware.
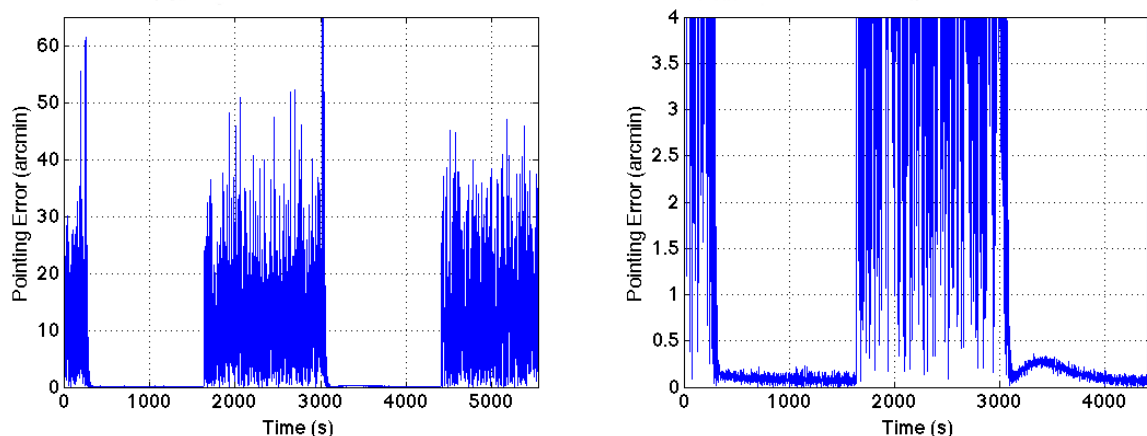

Figure 17: Pointing error with sensor noise in the system. The plot on the right shows that the PID controller is able to maintain a pointing accuracy of ¡0.5 arcmin despite the sensor noise.

Sensor noise has a significant impact on pointing accuracy especially during eigenaxis control; Eq. (22) shows how this control mode is directly susceptible to noise from both the STR and IMU. In this example performance requirements are still met after switching as the PID maintains an accuracy of 0.5 arcmin. However, in a more realistic scenario an IMU samples at a much faster rate than a STR so attitude estimate propagation would still be affected by IMU noise, decreasing the PID performance. This issue accentuates the need of a measurement propagation filter or EKF (extended Kalman Filter).

To address the issue of model fidelity and hardware-in-the-loop (HIL) testing , a real-time processing platform, the dSPACE-DS1006, has been acquired. This platform enables real-time testing of complex processes and models which would be too slow to run on a single computer. It also permits HIL testing of other subsystems within an orbital scenario, parallel to the satellite model.

V. Conclusion

The purpose of this paper has been to demonstrate the validity of the ADCS design approach as well as the capability of CubeSat class satellites to contribute to current areas of interest using COTS products and without the necessity of a multi-million dollar budget.

Proven models and methods are combined to produce an orbital environment detailed enough to run accurate, close range, relative orbit simulations including all significant disturbance sources at LEO altitude. The set-up is flexible enough to accept command profiles from external sources, allowing simulations of different maneuver scenarios. A switching control system design capable of extending point tracking performance over different operational modes is shown to maintain the required accuracy of 1 arcmin within the parameters of a 250 m relative orbit. Different switching schemes designed to improve transition smoothness, including bump conditioning and gain scheduling, are described in detail. Furthermore, a control system for a 6U CubeSat based on RCS thruster actuation was compared to a system based on RW actuation with thruster off-loading for the same satellite. The pointing accuracy and propellant consumption of the two

American Institute of Aeronautics and Astronautics

were found to be comparable, thus eliminating the need for RWs in the ARAPAIMA mission ADCS design and supporting the idea of a redundant propulsion system.

Transcending the scope a feasibility analysis, the aim is to prove, through simulation and testing, the performance of a system design that is able to extend into hardware integration and implementation. The current design prepares for this by respecting hardware limitations and accounting for the specifications of sensors and actuators such as sampling rates and thrust/mass-flow relations respectively. Future and current works focus on extending the compatibility of the existing model to include HIL and real-time testing.

Acknowledgments

References

[1]Harris, K., McGarvey, M., Chang, H. Y., Ryle, M., II, T. R., and Udrea, B., "Application for RSO Automated Proximity Analysis and IMAging (ARAPAIMA): Development of a Nanosat-based Space Situational Awareness Mission," *SmallSat 2013*, AIAA, August 2013.

[2]Shuster, M. D., "A Survey of Attitude Representations," *The Journal of the Astronautical Sciences*, Vol. 41, No. 4, October-December 1993, pp. 439–517.

[3]Simulink, M. ., *Aerospace Blockset User's Guide 2013a*, The MathWorks Inc., Natick, Massachusetts, 3rd ed., March 2013.

[4]Wertz, J. R., Everett, D. F., and Puschell, J. J., *Space Mission Engineering: The New SMAD*, Microcosm Press, 4th ed., 2011.

[5]Schutz, B., Tapley, B., and Born, G. H., *Statistical Orbit Determination*, Elsiever Academic Press, 2004.

[6]MATLAB, *Aerospace Toolbox User's Guide 2013a*, The MathWorks Inc., Natick, Massachusetts, 2nd ed., March 2013.

[7]Hedin, A. E., "MSIS-E-90 Atmoshpere Model," .

[8]Picone, M., Hedin, A., and Drob, D., "NRLMSISE-00," .

[9]Bird, G. A., *Molecular Gas Dynamics And The Direct Simulation Of Gas Flows*, Oxford University Press, USA, 1994.

[10]Maus, S., Macmillan, S., McLean, S., Hamilton, B., Thomson, A., Nair, M., and Rollins, C., "The US/UK World Magnetic Model for 2010-2015," Tech. rep., NOAA NESDIS/NGDC, 2010.

[11]Inamori, T., Sako, N., and Nakasuka, S., "Compensation of time-variable magnetic moments for a precise attitude control in nano-and micro-satellite missions," *Advances in Space Research*, Vol. 48, No. 3, 2011, pp. 432–440.

[12]Curtis, H., *Orbital Mechanics for Engineering Students*, Elsiever Aerospace Engineering Series, Butterworth-Heinemann, 3rd ed., 2013.

[13]Dodge, F. T., *The New Dynamic Behavior of Liquids in Moving Containers*, Southwest Research Institute, 2010.

[14]Huang, A., "Solenid Valve Linear Operation Region," Personal Communication, February 2014.

[15]Wie, B., Weiss, H., and Arapostathis, A., "Quaternion Feedback Regulator for Spacecraft Eigenaxis Rotations," *Journal of Guidance, Control, and Dynamics*, Vol. 12, No. 3, May-June 1989, pp. 375–380.

[16]Pong, C. M., Lim, S., Smith, M. W., Miller, D. W., Villaseñor, J. S., and Seager, S., "Achieving high-precision pointing on ExoplanetSat: Initial Feasibility Analysis," *MIT Open Access Articles*, 2010.

[17]Wie, B., "Quaternion Feedback For Spacecraft Large Angle Maneuvers," *Journal of Guidance, Control, and Dynamics*, Vol. 8, No. 3, 1985, pp. 360–365.

[18]Wie, B. and Lu, J., "Feedback Control Logic for Spacecraft Eigenaxis Rotations Under Slew Rate and Control Constraints," *Journal of Guidance, Control, and Dynamics*, Vol. 18, No. 6, 1995, pp. 1372–1379.

[19]Peng, Y., Vrancic, D., and Hanus, R., "Anti-Windup, Bumpless, and Conditioned Transfer Techniques for PID Controllers," *Control Systems, IEEE*, Vol. 16, No. 4, 1996, pp. 48–57.